Applied Radiation and Isotopes 150 (2019) 1–13

Contents lists available at ScienceDirect

Applied Radiation and Isotopes

journal homepage: www.elsevier.com/locate/apradiso

Locating lost radioactive sources using a UAV radiation monitoring system

Pin Gong[a], Xiao-Bin Tang[a,b,*], Xi Huang[a], Peng Wang[c], Liang-Sheng Wen[a], Xiao-Xiang Zhu[d], Cheng Zhou[d]

[a] Department of Nuclear Science and Engineering, Nanjing University of Aeronautics and Astronautics, 210016, Nanjing, China
[b] Jiangsu Engineering Laboratory of Nuclear Energy Equipment Materials, 210016, Nanjing, China
[c] School of Environmental and Biological Engineering, Nanjing University of Science and Technology, Nanjing, 210094, China
[d] Jiangsu Nuclear and Radiation Safety Supervision and Management Center, Nanjing, 210019, China

HIGHLIGHTS

- A novel source localization approach implemented by a UAV radiation detection instrument was proposed.
- Critical factors of the localization algorithm which could affect the localization accuracy were studied and discussed.
- Different experimental scenes such as the source on the grass, next to a tree, or in a puddle were applied and studied.
- A best result of 30 cm distance error was obtained in 0.1 s after a survey flight of 5 min within a $10 \times 10\,m^2$ range.

ARTICLE INFO

Keywords:
Lost source accidents
Source localization
UAV
Radiation monitoring system
Radiation detection

ABSTRACT

Locating lost radioactive sources quickly, precisely, and safely is very important in emergency responses of lost radioactive source accidents. This paper describes a source localization approach using an independently developed unmanned aerial vehicle (UAV) radiation monitoring system, which uses a specialized source localization algorithm. Once a radiation anomaly spot is found on the ground, an $L \times L$ (m^2) square area around the anomaly spot defined as suspicious region is selected to perform an accurate source localization. Then, the UAV radiation monitoring instrument is dispatched to hover at some scheduled detection positions within the suspicious region for radiation measurements. After the last hover finished, the actual source position is calculated by the source localization algorithm program in real time. The source localization algorithm was developed on the basis of the inverse-square law and statistical methods. Five critical factors of the algorithm that may lead to errors in localization such as the meshing number in calculations, the size of the suspicious region, the number of the detection positions, the distribution of the detection positions, and the coverage range of the detection positions were studied by using measurement data from Monte Carlo simulations. Subsequently, the approach was experimentally verified for a 3.7×10^7 Bq ^{131}I source localization. Three experimental scenes were applied such as the source on the grass, next to a tree, and in a puddle. Different distributions of the detection positions and different numbers of the detection positions were studied. The best localization distance error was 30 cm within a $10 \times 10\,m^2$ suspicious region, and the calculation time was not more than 0.1 s after a total survey flight of 5 min.

1. Introduction

A total of 253 radiation accidents occurred in China from 2004 to 2015. According to the Ministry of Environmental Protection of the PRC, 77.9% of these accidents were related to lost or stolen radioactive sources. Most of the lost sources were used in level gauges, densitometers, and flaw detectors, and the maximum activity of the lost sources was more than 3.7×10^{11} Bq, which is quite dangerous. Localization of the lost sources as soon as possible by some mobile surveys will reduce the risk of radiation harm to the public. Compared to other mobile surveys such as handheld, vehicle mounted, or human piloted, surveys by unmanned aerial vehicle (UAV) radiation monitoring systems can be conducted remotely; this can remove the possibility of endangering survey workers within high-dose radiation environments.

A variety of UAV designs have been developed for radiation

* Corresponding author. Department of Nuclear Science and Engineering, Nanjing University of Aeronautics and Astronautics, 210016, Nanjing, China.
E-mail address: tangxiaobin@nuaa.edu.cn (X.-B. Tang).

https://doi.org/10.1016/j.apradiso.2019.04.037
Received 12 December 2017; Received in revised form 18 March 2019; Accepted 30 April 2019
Available online 05 May 2019
0969-8043/

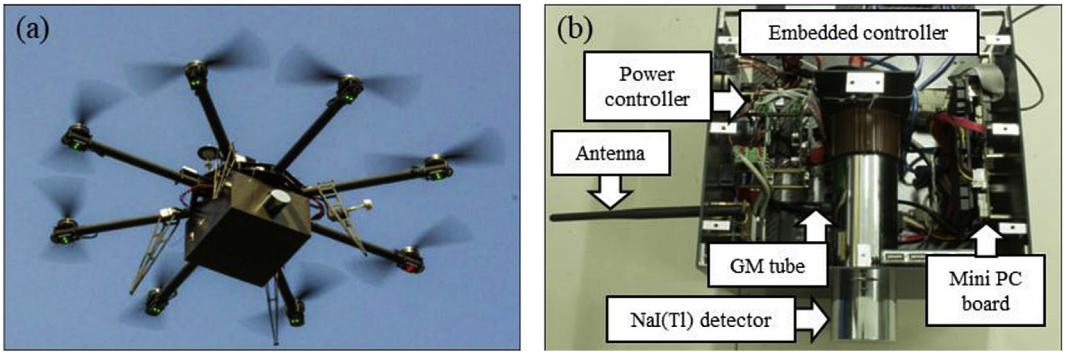

Fig. 1. (a) Overview of the RotorRAD radiation monitoring system. (b) Inner view of the integrated payload.

Table 1
Main physical and technical characteristics of the RotorRAD.

Characteristics	Value
System mass	< 15 kg
Dose rate range	0.1 μSv/h to 100 mSv/h
γ rays' energy range	20 keV to 3 MeV
Energy resolution at 662 keV	< 7%
Duration of flight	~30 min
Maximum transmission distance	5 km
Operating temperature	−20 °C to +40 °C

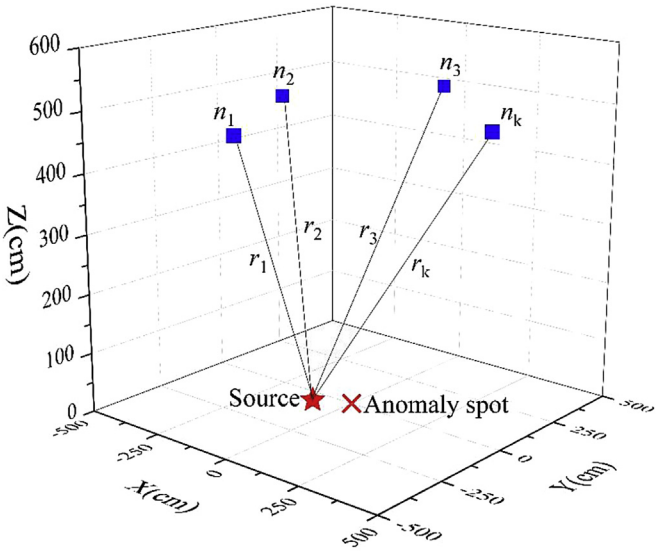

Fig. 2. Schematic of source localization. The detection positions are indicated by the solid blue squares. (For interpretation of the references to color in this figure legend, the reader is referred to the Web version of this article.)

surveying in previous studies, including fixed-wing (Pöllänen et al., 2009), single-rotor (Sanada and Torii, 2015), and multirotor UAVs (MacFarlane et al., 2014; Martin et al., 2015, 2016; Falciglia et al., 2017; Šálek et al., 2018). Among these aircrafts, multirotor UAVs that fly at low speed and altitude are more suitable for localizing a specific radioactive point source (Connor et al., 2016). At the same time, various types of gamma detectors are commonly employed in UAV radiation monitoring systems, such as Geiger–Muller (GM) tubes (Kurvinen et al., 2005), NaI detectors (Towler et al., 2012; Jerry et al., 2012; Casanovas et al., 2014), CsI detectors (Han and Chen, 2014), $LaBr_3$ detectors (Sanada and Torii, 2015; Huang et al., 2016), bismuth germanate (BGO) detectors (Šálek et al., 2018), and cadmium zinc telluride (CZT) detectors (Martin et al., 2015). A CZT detector provides a high energy resolution, but its counting efficiency is relatively low

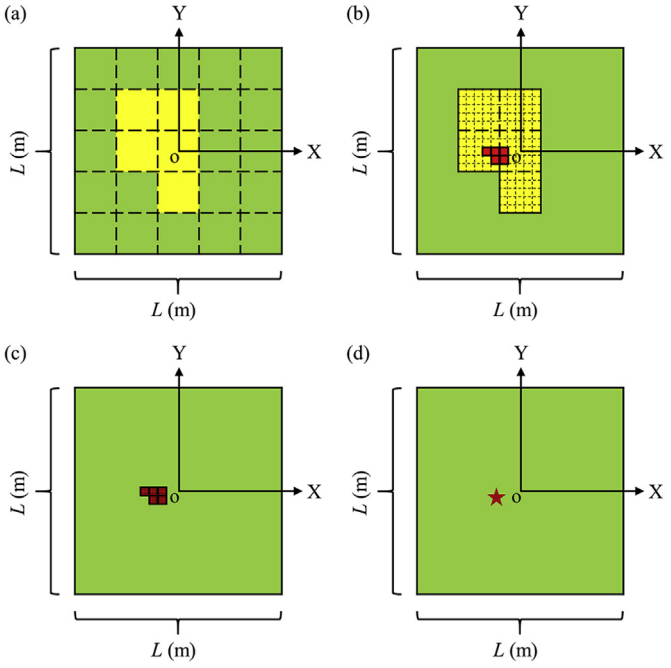

Fig. 3. Schematic of meshing operations in the source localization algorithm: (a) first meshing, (b) second meshing, (c) third meshing, and (d) calculation finished. The green area is the suspicious region. Meshing number $M = 5$. The red star indicates the calculated source position. (For interpretation of the references to color in this figure legend, the reader is referred to the Web version of this article.)

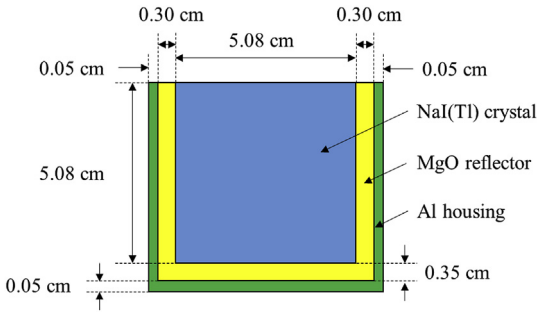

Fig. 4. MCNP model of the detector.

because of the limited volume of the CZT material, i.e., 1 cm^3 (Luke et al., 2001). The cost of NaI detector is lower than other scintillators and produces a greater photon brightness (Knoll, 2010). Therefore, it is cost effective to use a NaI detector in a UAV radiation monitoring system without a demand for high energy resolution.

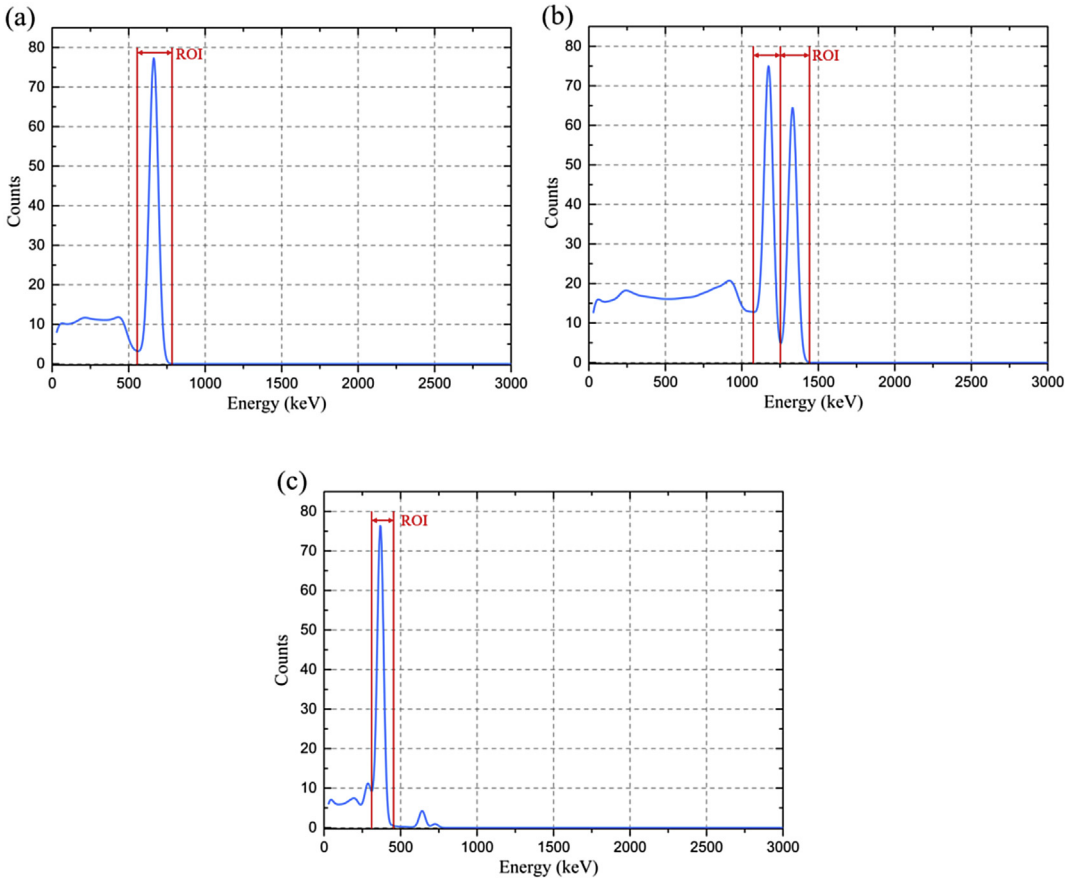

Fig. 5. Simulated spectra and the ROI selected: (a) ^{137}Cs, (b) ^{60}Co, and (c) ^{131}I.

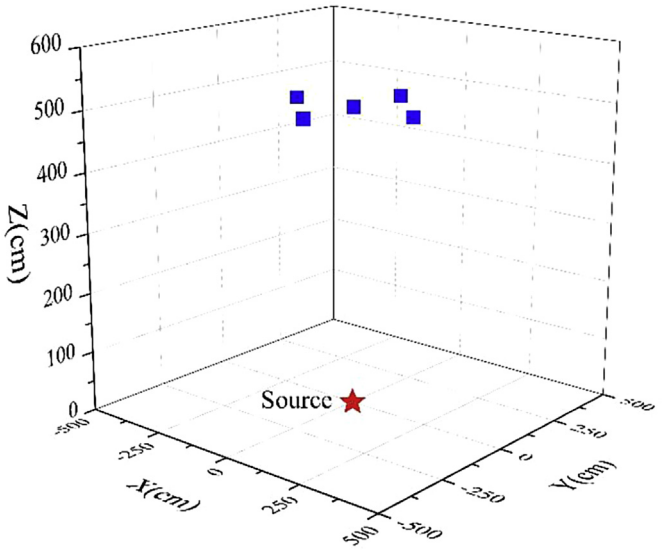

Fig. 6. Distribution of the detection positions in Case 1. The detection positions are indicated by the solid blue squares. (For interpretation of the references to color in this figure legend, the reader is referred to the Web version of this article.)

An efficient algorithm is the key for radioactive source localizations. Most of the source localization algorithms are based on the inverse square law and statistical methods. In previous works, four main types of algorithms have been studied, namely nonlinear least squares estimation algorithms (Howse et al., 2001), recursive Bayesian estimation (RBE) algorithms (Brewer, 2009; Towler et al., 2012), maximum likelihood estimation (MLE) algorithms (Gunatilaka et al., 2007; Morelande et al., 2007), and difference of time-of-arrival (DTOA) algorithms (Xu et al., 2010; Rao et al., 2015). Some other researchers employed multiple detectors to locate a point source in two-dimensional or three-dimensional spaces (Willis et al., 2014; Hanna et al., 2015; Sharma et al., 2016).

In 2016, a UAV radiation monitoring system (RotorRAD) was developed by our group for radiation surveying and radioactive source localization. A specific source localization algorithm programmed with Visual Studio was applied to the system, and the performances of the algorithm with different input variables were studied in this work by simulation and experimental methods.

2. Materials and methods

2.1. Description of the RotorRAD radiation monitoring system

The picture of the RotorRAD radiation monitoring system is shown in Fig. 1. The system consists of a multirotor (eight propellers) aerial vehicle and an integrated detection payload, which consists of a 2" × 2″ NaI(Tl) scintillation detector (model 905–3, ORTEC) with a multichannel analyzer (MCA), a GM detector (model 7807, LND), a GPS, a RF antenna, a power controller, an embedded controller, and a Windows Mini PC board. The usage of a NaI(Tl) detector is cost effective compared with other detectors used in UAV radiation detection systems such as $LaBr_3$, CZT, and BGO at the same detection efficiency. The NaI(Tl) scintillation detector employed here can measure γ energy range from 20 keV to 3 MeV, which covers most of the common artificial radioactive nuclides. The pulse signals of the detector during measurements are analyzed using a 1024-channel MCA to produce a spectrum for source localization calculations. Because the RotorRAD

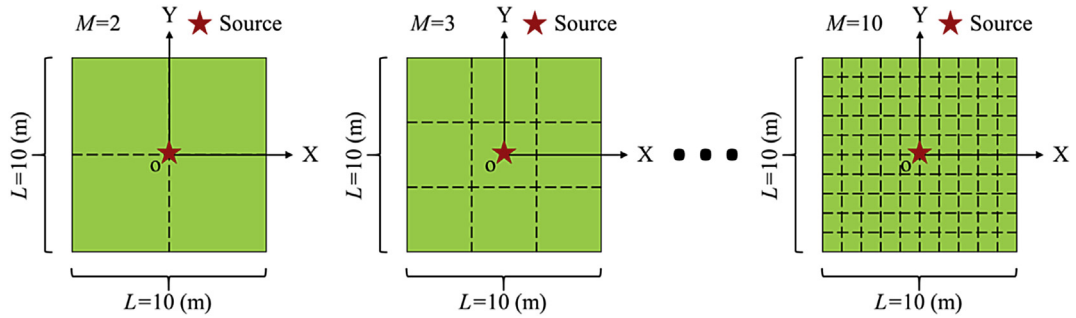

Fig. 7. Schematic of Case 1: changing the meshing number *M*.

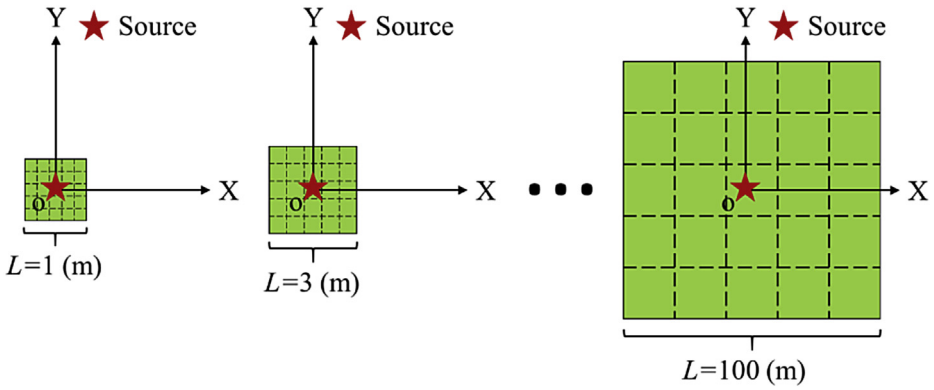

Fig. 8. Schematic of Case 2: changing the size of the suspicious region.

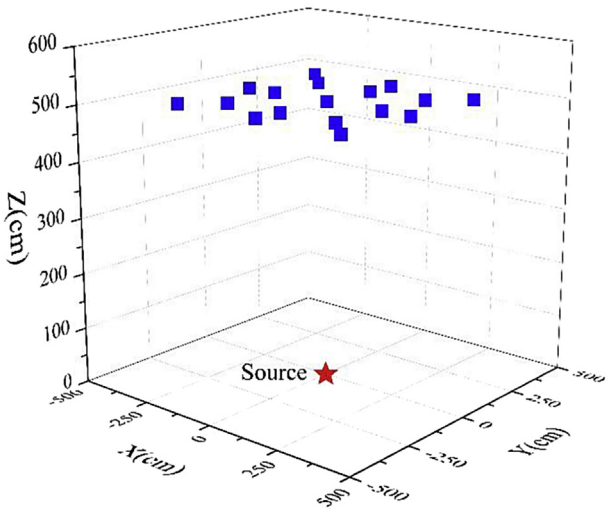

Fig. 9. Distribution of the detection positions in Case 3. The detection positions are indicated by the blue squares. (For interpretation of the references to color in this figure legend, the reader is referred to the Web version of this article.)

radiation monitoring system can also be used for dose rate monitoring, a GM detector is built in for high dose rate measurements and functions when the NaI(Tl) detector does not respond properly in some strong radiation environments.

Two 22000-mAh lithium cells are mounted on the vehicle. The duration of each survey flight is approximately 30 min. The batteries should be changed before starting another flight. During each flight, the dose rates, gamma spectra, GPS positions, and other collected data are stored locally in the instrument and concurrently transmitted to an on-ground terminal for real-time analysis. Theoretically, the proposed system can fly at altitudes above 100 m. However, near-surface flights are usually implemented in practical surveys to increase the sensitivity of radiation detections. The major characteristics of the RotorRAD are listed in Table 1.

2.2. Radioactive source localization algorithm

A wide range of radiation surveys are usually performed after a lost radioactive source accident is reported. When a radioactive anomaly is found at a search spot, which indicates the possible presence of the source nearby, the RotorRAD can be used for a fast and accurate localization of the lost source. The routine procedure of the source localization using the RotorRAD is as follows. (a) The ground spot that reports anomaly is set as the coordinate origin, and an $L \times L$ (m^2) square area that is centered at the origin in the ground plane is selected as the suspicious region for the localization. (b) The RotorRAD is dispatched to fly over the suspicious region. (c) The RotorRAD hovers at N scheduled detection positions and acquires and transmits gamma spectra data from the detector to the on-ground terminal. (d) The source position is calculated by a computer program using the localization algorithm. Fig. 2 shows the schematic diagram of the procedure.

Assume that the actual position of the lost source in the ground plane is known as shown in Fig. 2. For simplicity, we also assume that no gamma ray attenuation by the air occurs between the source and the detector. According to basic radiation detection theory (Knoll, 2010), the count rate in the full-energy peak of the spectrum at each detection position is as follows:

$$n_k = Af\frac{a}{4\pi {r_k}^2}\varepsilon_P,\ k = 1,2,\ \ldots,N \tag{1}$$

where n_k is the background subtracted count rate under the full-energy peak in the spectrum at each detection position, A is the activity of the source, f is the decay fraction of the total disintegration in which the measured gamma ray is emitted, a is the effective sensitive area of the detector toward the source, r_k is the source-to-detector distance at each detection position, and ε_P is the intrinsic peak efficiency.

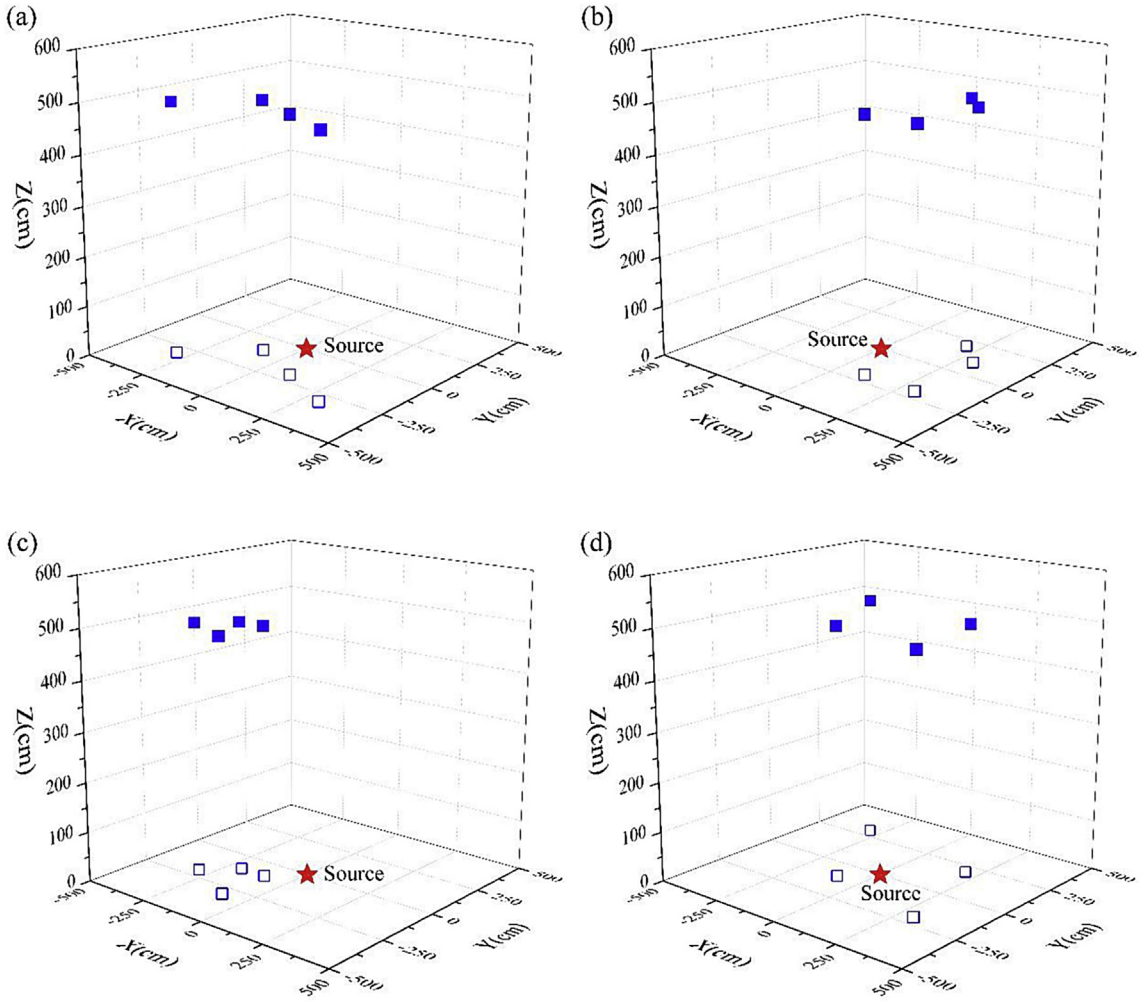

Fig. 10. Distributions of the detection positions in Case 4. The XY projections of the detection positions were in (a) quadrants of 3–4, (b) quadrants of 1–4, (c) quadrants of 3, and (d) quadrants of 1-2-3-4. The detection positions and their XY projections are indicated by the solid blue squares and the hollow blue squares, respectively. The actual source position is indicated by the solid red star. (For interpretation of the references to color in this figure legend, the reader is referred to the Web version of this article.)

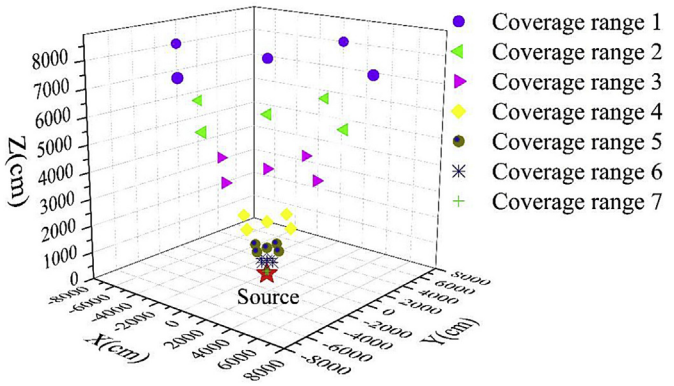

Fig. 11. Distributions of the detection positions with different coverage ranges in Case 5. The detection positions are indicated by the colored symbols. The actual source position is indicated by the solid red star. (For interpretation of the references to color in this figure legend, the reader is referred to the Web version of this article.)

$$n_k r_k^2 = Af\frac{a}{4\pi}\varepsilon_P,\ k = 1,2,\ \ldots,N \tag{2}$$

In Eq. (2), the activity A of the source may be regarded as a constant because the localization time is usually much shorter than the half-life of the source. Thus, $n_k r_k^2$ remains unchanged because the other parameters f, a, and ε_P are also constant during the localization process. Theoretically, the standard deviation of N $n_k r_k^2$ values would be zero if the detection uncertainties are negligible, that is,

$$\sigma(n_1 r_1^2,\ n_2 r_2^2, \ldots, n_N r_N^2) = 0 \tag{3}$$

In a real situation, the actual source position is unknown, and any position in the ground plane may be calculated to generate a σ of $n_k r_k^2$ values. From these positions, the closer the σ is to zero, the closer is the position to the actual source position.

As the final step of the source localization procedure mentioned above, the $L \times L$ (m^2) suspicious region is first meshed by $M \times M$ square cells as shown in Fig. 3(a). M is the meshing number, and here, let $M = 5$ for illustrations in Fig. 3. Then, the geometric center of every cell, $(x_i, y_i, 0)$, $(i = 1,2,\ldots,M^2)$, is regarded as a test position. Total M^2 test positions are considered in the first meshing. If the coordinate of the k-th detection position that corresponds to the count rate n_k is (x_k, y_k, z_k), the square of a distance from the i-th test position $(x_i, y_i, 0)$ to the k-th detection position (x_{ik}, y_{ik}, z_{ik}) is

$$r_{ik}^2 = (x_{ik} - x_i)^2 + (y_{ik} - y_i)^2 + z_{ik}^2,\ k = 1,2\ldots,N \tag{4}$$

There are N r_{ik}^2 followed by a standard deviation $\sigma_i(n_1 r_{i1}^2,\ n_2 r_{i2}^2, \ldots, n_N r_{iN}^2)$ corresponding to each test position $(x_i, y_i, 0)$. After the calculations of all σ_i for M^2 test positions, the minimum M σ

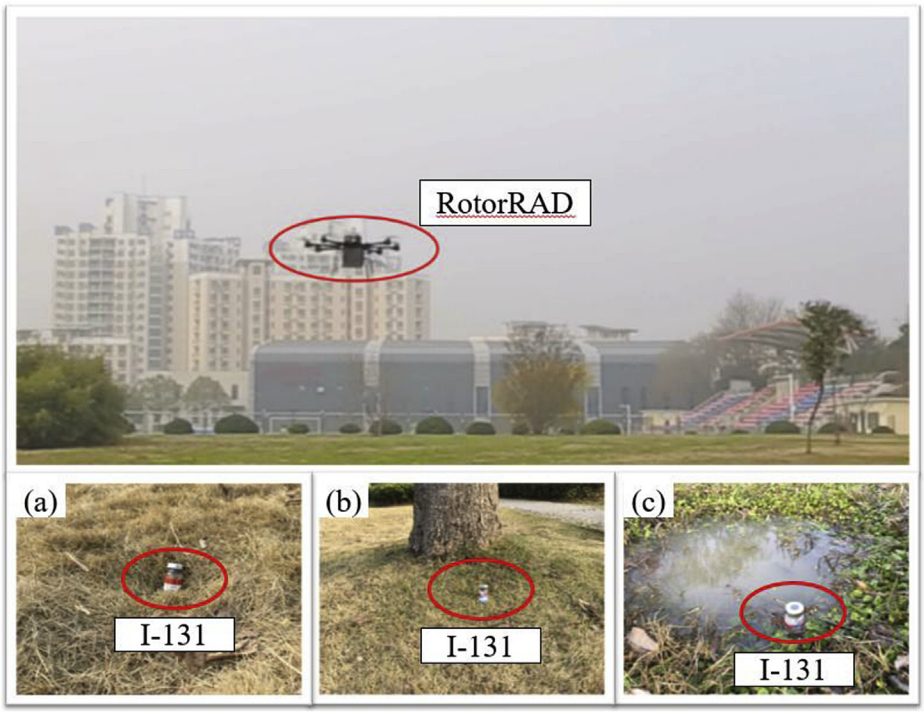

Fig. 12. Scenes of the experimental field. (a) Scene A: ^{131}I placed on the grass, (b) Scene B: ^{131}I placed next to a tree, and (c) Scene C: ^{131}I placed in a puddle.

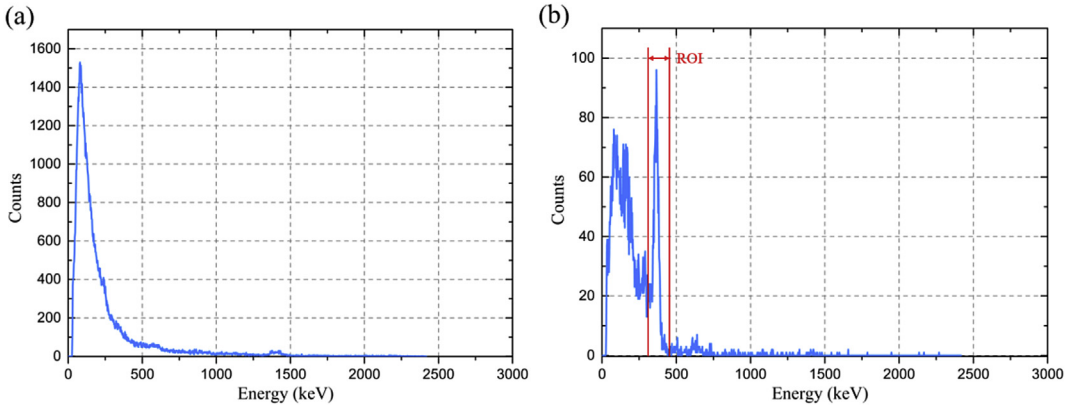

Fig. 13. (a) 10-min background spectrum; (b) 10-s ^{131}I spectrum.

values are stored in array S_1, and the corresponding M cells are selected for the second meshing operation, that is, the five yellow cells in Fig. 3(a). The selected cells are then meshed by $M \times M$ smaller cells separately, thus generating M^3 new test positions as shown in Fig. 3(b). σ_i is calculated at each test position. The minimum M σ values are stored in array S_2, and the corresponding M cells are selected for the third meshing operation, that is, the five red cells in Fig. 3(c), thereby generating M^3 new test positions. Meshing operations are repeated to produce arrays S_3, S_4, …, S_{n-1}, S_n in succession until $S_n = S_{n-1}$, and the test position in S_n with minimum σ is recorded as the actual source position, which is shown by the red star in Fig. 3(d). This source localization algorithm was programmed using Visual Studio and successfully implemented.

2.3. Method of simulation research

The positioning accuracy of the source and the calculation time using the source localization algorithm are influenced by some factors such as the meshing number M, the length of the suspicious region L, the number of the detection positions N, the distribution of the detection positions, and the coverage range of the detection positions. The performances of the source localization algorithm in five different cases corresponding to the abovementioned affecting factors were studied by simulation methods.

As a useful Monte Carlo simulation tool, MCNP (Brown, 2003; Gong et al., 2014) was used to simulate the gamma spectra response of the RotorRAD and produce the count rate data n_k for source-positioning calculations in different cases. A 2" × 2" NaI(Tl) scintillation detector was modeled in the MCNP using the same specifications as the RotorRAD detector (see Fig. 4 for detail). The materials and dimension data of the detector were provided by the detector manufacturer. The detector was surrounded by air, and a point source was modeled in the MCNP. ^{137}Cs was used in cases 1 to 4, while ^{60}Co and ^{131}I were used in case 5 in addition to ^{137}Cs. Simulation results showed that the activity of each type of source was 1×10^9 Bq. Furthermore, the time of measurement at every detection position in all the cases was assumed as 10 s. Fig. 5 shows the simulated spectra of ^{137}Cs, ^{60}Co, ^{131}I, and the regions of interest (ROI) selected.

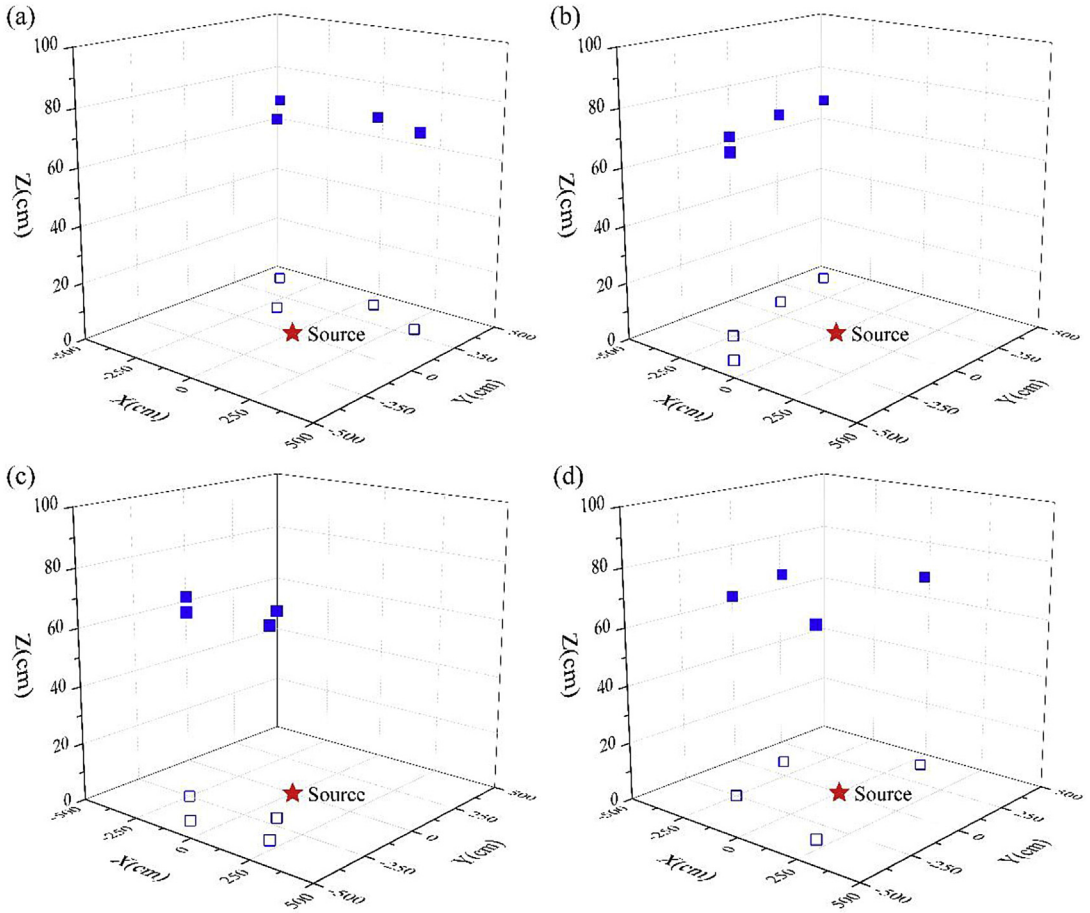

Fig. 14. Distributions of the detection positions in Scenes A and B. The XY projections of the detection positions were in (a) quadrants of 1–2, (b) quadrants of 2–3, (c) quadrants of 3–4, and (d) quadrants of 1-2-3-4. The detection positions and their XY projections are indicated by the solid blue squares and hollow blue squares, respectively. The actual source position is indicated by the solid red star. (For interpretation of the references to color in this figure legend, the reader is referred to the Web version of this article.)

2.3.1. Case 1: Changing the meshing number M

In this case, the source positioning errors and the calculation time with different meshing numbers *M*, which dictates the number of the meshed cells in every meshing operation, were studied. The suspicious region was set to 10 × 10 m^2. The coordinate of the actual source was set to (0,0,0) cm. Five detection positions over the suspicious region at an altitude of 5 m were distributed as shown in Fig. 6. Nine situations were studied, where *M* was set to 2, 3, 4, 5, 6, 7, 8, 9, and 10 as shown in Fig. 7.

2.3.2. Case 2: Changing the size of the suspicious region

In this case, the source positioning errors and the calculation time with different suspicious region sizes were studied. The coordinate of the actual source was set to (0,0,0) cm, the detection positions were the same as in Fig. 6, and the meshing number *M* was set to 5. Eight situations were studied, where the length of suspicious region *L* was set to 1, 3, 6, 10, 20, 50, 80, and 100 m as shown in Fig. 8.

2.3.3. Case 3: Changing the number of the detection positions

In this case, the source positioning errors with different numbers of the detection positions were studied. The suspicious region was set to 10 × 10 (m^2), and the meshing number *M* was set to 5. The coordinate of the actual source was set to (0,0,0) cm, and the 17 detection positions used in case 3 were distributed as shown in Fig. 9 at an altitude of 5 m. Eight situations were studied, and the number of the detection positions were 3, 4, 5, 6, 7, 8, 9, and 10. For each number of the detection positions, four different position combinations were randomly selected from 17 positions, and the corresponding source positioning results were averaged.

2.3.4. Case 4: Changing the distribution of the detection positions

In this case, the source positioning errors with different distributions of the detection positions were studied. The suspicious region was set to 10 × 10 (m^2), and the meshing number *M* was set to 5. The coordinate of the actual source was set to (0,0,0) cm. Four kinds of distributions of the detection positions over the suspicious region were selected at an altitude of 5 m to implement source positioning calculations. The XY projections of the detection positions in these four distributions were in quadrants 3–4, 1–4, 3, and 1-2-3-4 in the XY plane, as shown in Fig. 10.

2.3.5. Case 5: Changing the coverage range of the detection positions

The distance between the actual source and the detection positions increases when an enlarged coverage range of the detection positions with a high altitude is implemented. The inverse-square effect and high gamma ray attenuation by the air with longer distance will decline the count rates of the detector, which means more statistics fluctuations and less precision of measurements. To evaluate the impact on the accuracy of source positioning under this situation, the source positioning errors with different coverage ranges of the detection positions were studied. In addition to ^{137}Cs, ^{60}Co and ^{131}I were simulated considering different attenuation effects at different gamma energies. The suspicious region was set to 10 × 10 (m^2), and the meshing number *M* was set to 5. The coordinate of the actual source was set to (0,0,0) cm.

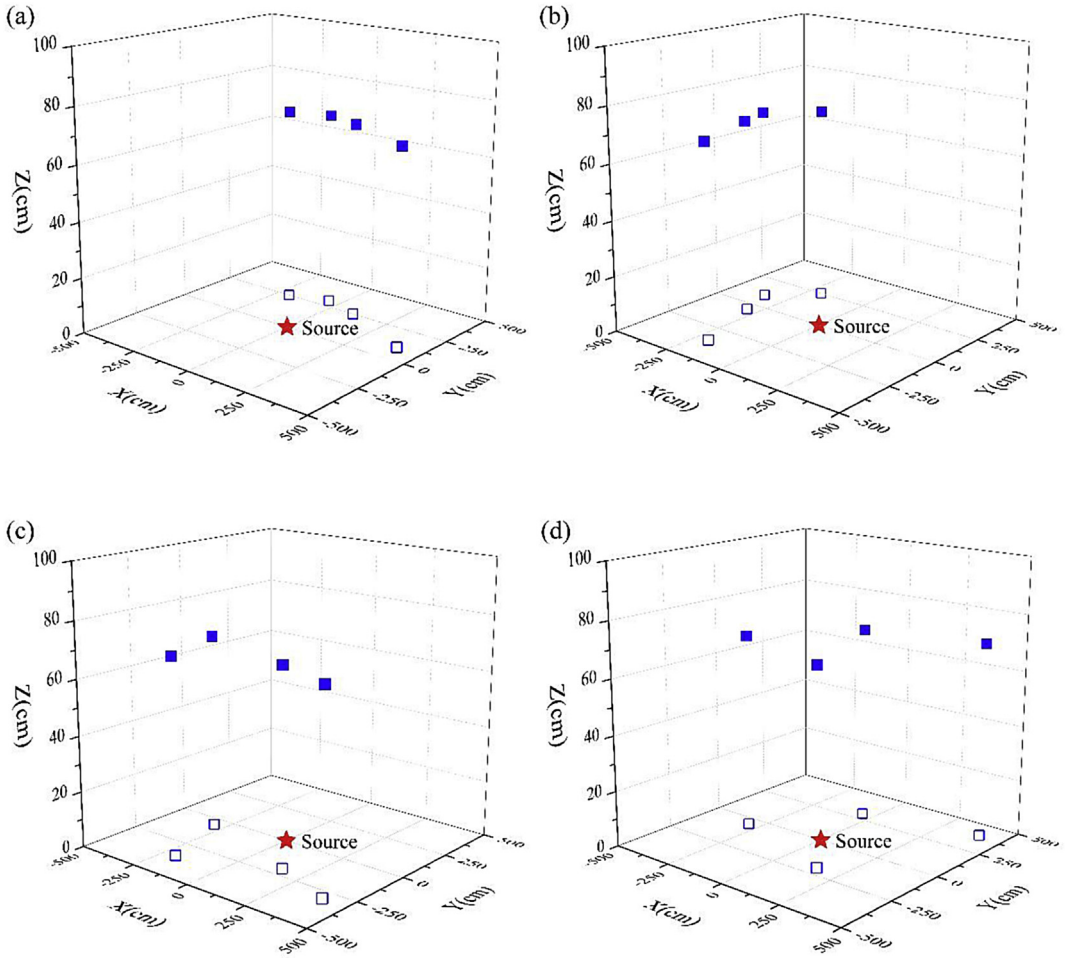

Fig. 15. Distributions of the detection positions in Scene C. The XY projections of the detection positions were in (a) quadrants of 1–2, (b) quadrants of 2–3, (c) quadrants of 3–4, and (d) quadrants of 1-2-3-4. The detection positions and their XY projections are indicated by the solid blue squares and hollow blue squares, respectively. The actual source position is indicated by the solid red star. (For interpretation of the references to color in this figure legend, the reader is referred to the Web version of this article.)

Table 2
Coordinates of the detection positions relative to the actual source position in the experiment of Scenes A and B. DP represents the detection position.

DP	x (cm)	y (cm)	z (cm)	DP	x (cm)	y (cm)	z (cm)
1	350	50	70	6	−200	150	70
2	300	300	70	7	−250	−250	70
3	50	400	70	8	−100	−400	70
4	−400	400	70	9	200	−350	70
5	−350	100	70	10	100	−200	70

Table 3
Coordinates of the detection positions relative to the actual source position in the experiment of Scene C. DP represents the detection position.

DP	x (cm)	y (cm)	z (cm)	DP	x (cm)	y (cm)	z (cm)
1	−350	100	70	6	400	100	70
2	−200	250	70	7	−300	−50	70
3	−50	300	70	8	−200	−350	70
4	100	250	70	9	150	−200	70
5	400	400	70	10	400	−300	70

Seven combinations of detection positions with different coverage ranges from $0.2 \times 0.2\,m^2$ to $160 \times 160\,m^2$ at altitudes from 0.1 m to 80 m were studied. The distributions of the detection positions used in Case 5 are shown in Fig. 11.

2.4. Method of experimental research

An ^{131}I source of activity 3.7×10^7 Bq was used to verify the validity of the proposed source localization algorithm. Three different experimental scenes were performed in the campus of Nanjing University of Aeronautics and Astronautics. As shown in Fig. 12, the first scene (Scene A) is locating a source placed on the grass, the second scene (Scene B) is locating a source placed next to a tree, and the third scene (Scene C) is locating a source placed in a puddle. Before experiments, a 10-min background spectrum was measured at an altitude of 0.7 m above the experimental field without any radioactive source around using the RotorRAD radiation monitoring system. Fig. 13 shows the acquired background spectrum and one of the ^{131}I spectra. The net count rates n_k of all the detection positions in Scene A were between 81 cps and 323 cps, and similar count levels were acquired in Scenes B and C.

For each scene, the experimental procedures were carried out as follows. (a) The source was placed in the scene spot. (b) The position of the source was considered as the coordinate origin (0,0,0) cm. (c) A 10×10 (m^2) suspicious region centered on (0,0,0) and a meshing number of $M = 5$ were set. (d) The RotorRAD radiation monitoring system was set to hover at some detection positions with an altitude of 0.7 m within the suspicious region. (e) A background subtracted 10-s gamma spectrum was acquired for each detection position and used to calculate the count rate data n_k. (f) The source position was calculated automatically by the localization software after the last detection

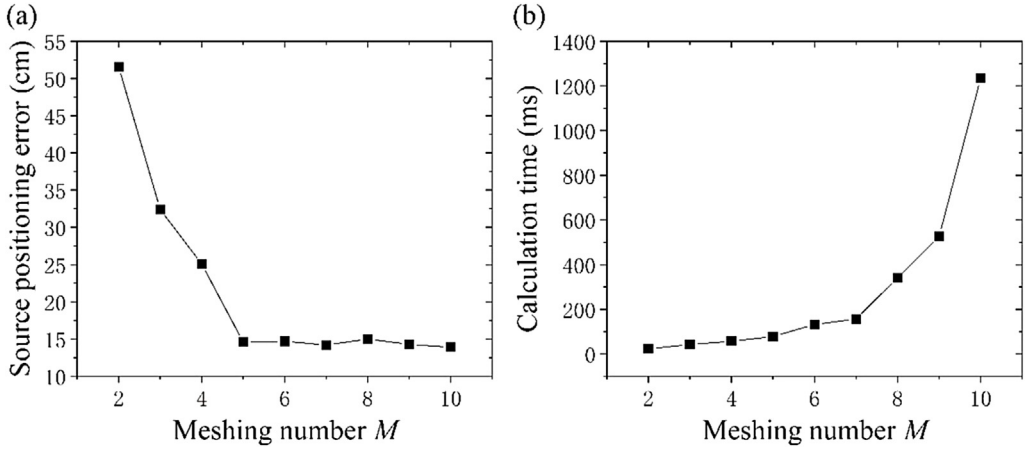

Fig. 16. Source positioning errors and calculation time with different meshing numbers *M*.

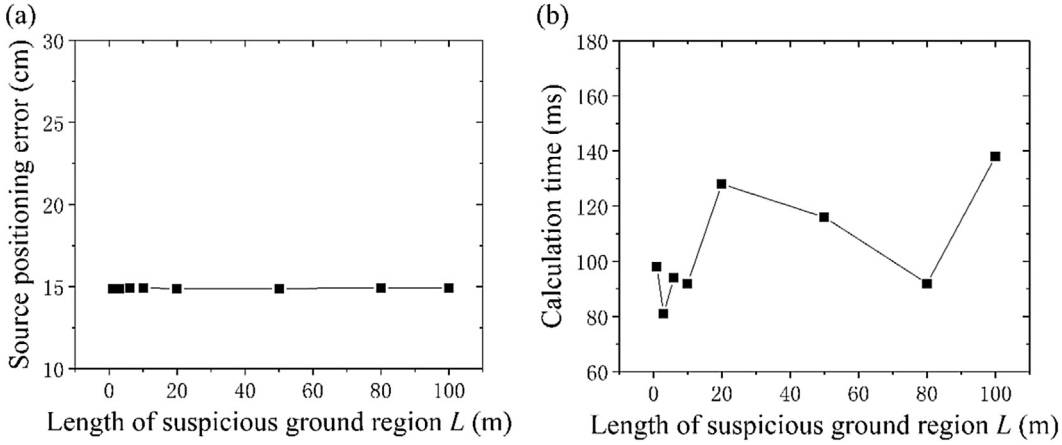

Fig. 17. Source positioning errors and calculation time with different lengths of suspicious region *L*.

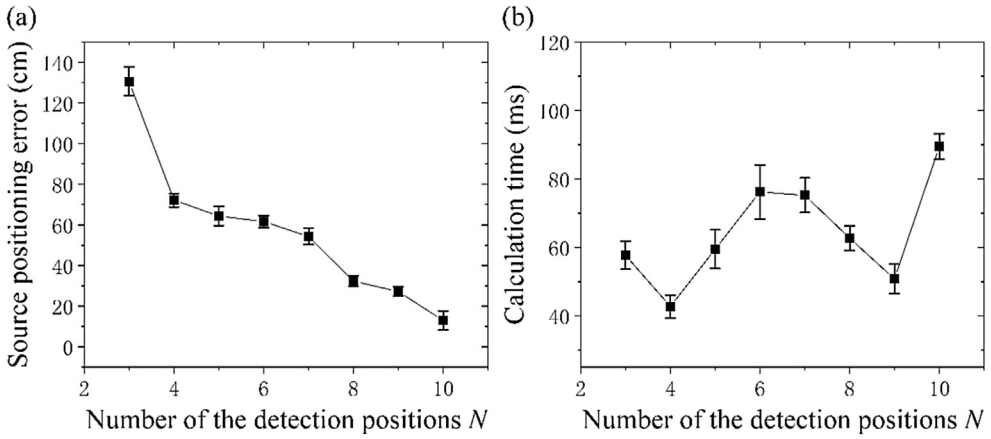

Fig. 18. Source positioning errors and calculation time with different numbers of detection positions.

finished. For each scene, four distributions of the detection positions were studied. The XY projections of the detection positions in these distributions were in quadrants 1–2, 2–3, 3–4, and 1-2-3-4 in the XY plane, as shown in Fig. 14 (Scenes A and B) and Fig. 15 (Scene C). The coordinate of the tree (Scene B) was (0,-50,0) cm.

For each scene, different numbers of the detection positions were also studied. Ten detection positions were performed, of which 5, 6, 7, 8, 9, 10 detection positions were used to calculate the positions of the source. The coordinates of the 10 detection positions are listed in Table 2 (Scenes A and B) and Table 3 (Scene C).

3. Results and discussion

3.1. Simulation results

Fig. 16 shows the results of the source positioning errors and the calculation time with different meshing numbers *M* in simulation research Case 1. The source positioning errors (cm) represent the distances between the actual source position and the calculated source positions obtained by the localization algorithm. Fig. 16(a) shows that the source positioning errors decreased rapidly from 52 cm to 15 cm as

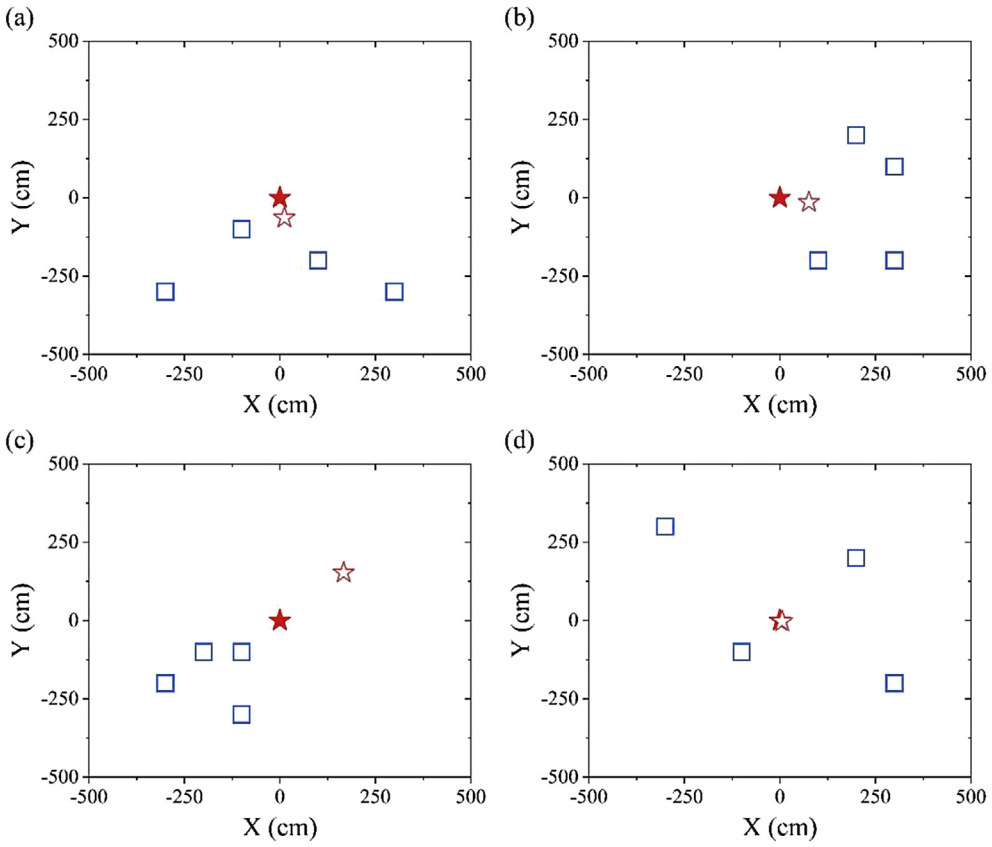

Fig. 19. Calculated source positions with different distributions of the detection positions. The detection positions were (a) focused on one side of the Y axis, (b) focused on one side of the X axis, (c) focused on one side of the X axis and one side of the Y axis, and (d) dispersed around the source. The XY projections of the detection positions are indicated by the blue squares. The actual source position is indicated by the solid red star, and the calculated source position is indicated by the hollow red star. (For interpretation of the references to color in this figure legend, the reader is referred to the Web version of this article.)

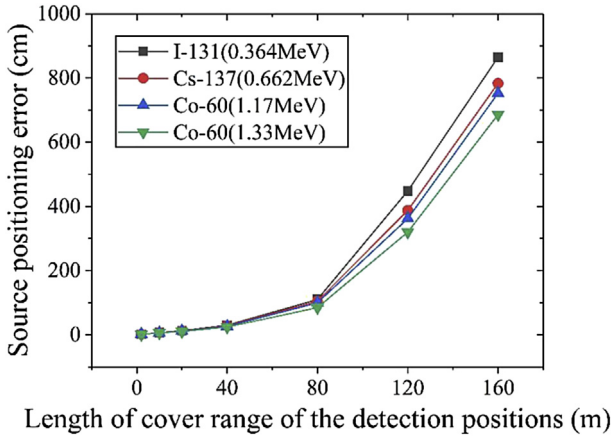

Fig. 20. Source positioning errors with different coverage ranges of the detection positions.

M increased from 2 to 5, and the errors remained stable as *M* continuously increased to 10. Theoretically, the finer the cells are meshed in every meshing operation, the more accurate the source position obtained will be. However, the minimum distance between the source position and the detection positions limited by the flight height, which was about 5 m in Case 1, determined a floor of the positioning errors. As shown in Fig. 16(b), the calculation time of the localization increased from 23 ms to 1234 ms as *M* increased from 2 to 10. Therefore, *M* was appropriately set to 5, thereby achieving an efficient positioning precision in the least possible calculation time under similar detection conditions as in Case 1.

Fig. 17 shows the results of the source positioning errors and the calculation time with different suspicious region sizes in simulation research Case 2. The source positioning errors were constant at 15 cm as the length of the suspicious region *L* changed from 1 m to 100 m, and the calculation time fluctuated from 80 ms to 140 ms. The largest *L* should be selected considering the maximum detectable distance of the target source for localization efficiency because the size of the suspicious region has no effect on source positioning accuracy and negligible impact on calculation time.

Fig. 18 shows the results of the source positioning errors and the calculation time with different numbers of detection positions *N* in simulation research Case 3. The positioning errors continuously decreased from 130.6 cm to 12.9 cm as the *N* increased from 3 to 10. Furthermore, the calculation time fluctuated between 40 ms and 90 ms; this indicates that more detection positions should be implemented to achieve adequate positioning accuracy without the need for considering the additional calculation time consumption.

Fig. 19 shows the results of the calculated source positions with different distributions of the detection positions in simulation research Case 4. For distribution (1) in Fig. 19(a), the detection positions were dispersed on both sides of the Y axis and focused on one side of the X axis, resulting in 12 cm of X error and 64 cm of Y error. For distribution (2) in Fig. 19(b), the detection positions were dispersed on both sides of the X axis and focused on one side of the Y axis, resulting in 76 cm of X error and 14 cm of Y error. For distribution (3) in Fig. 19(c), the detection positions were focused on one side of the X axis and one side of the Y axis, resulting in 167 cm of X error and 153 cm of Y error. For distribution (4) in Fig. 19(d), the detection positions were dispersed on both sides of the X axis and both sides of the Y axis, resulting in 6 cm of X error and 3 cm of Y error. Keeping the source in the coverage range of the detection positions will result in a more accurate calculated source position. As the actual source position is unknown before the detections, dispersing the detection positions around the suspicious region selected will help in increasing the probability of covering the actual source by the detection positions and increase the accuracy of the source positioning calculations. Furthermore, once a positioning result shows that the calculated source position is out of the coverage region

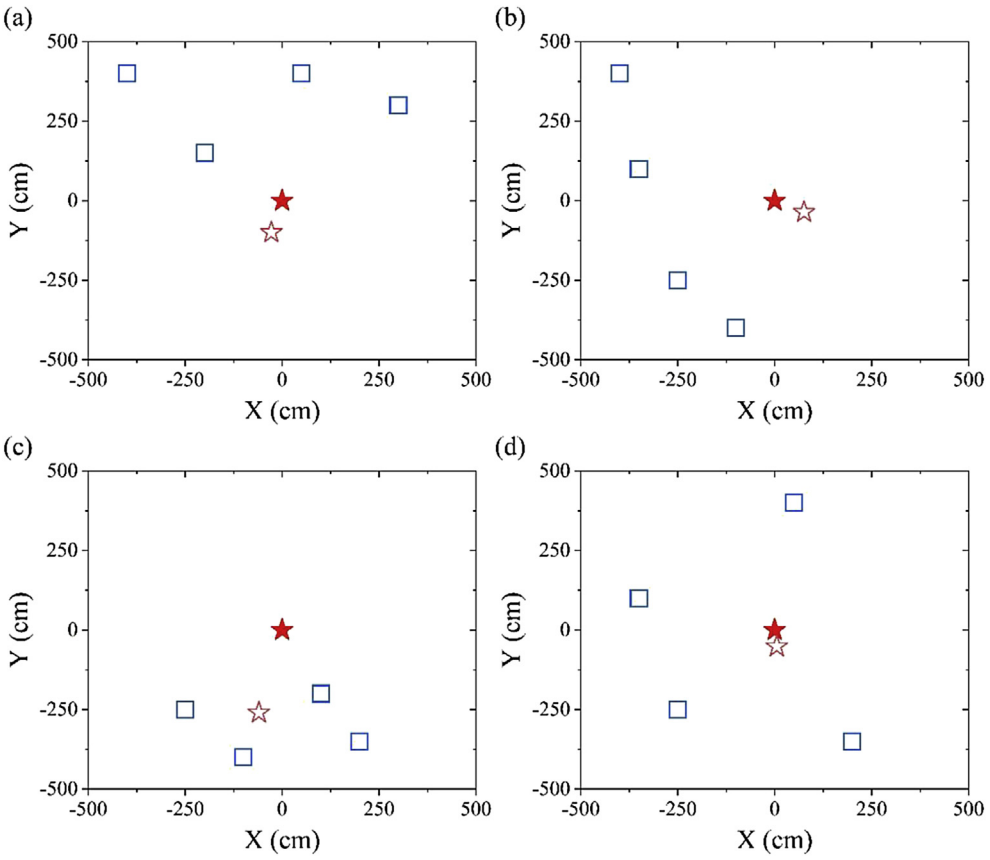

Fig. 21. Calculated source positions with different distributions of the detection positions in Scene A. The detection positions were (a–c) focused on one side of the X axis or the Y axis and (d) dispersed around the source. The XY projections of the detection positions are indicated by the blue squares. The actual source position is indicated by the solid red star, and the calculated source position is indicated by the hollow red star. (For interpretation of the references to color in this figure legend, the reader is referred to the Web version of this article.)

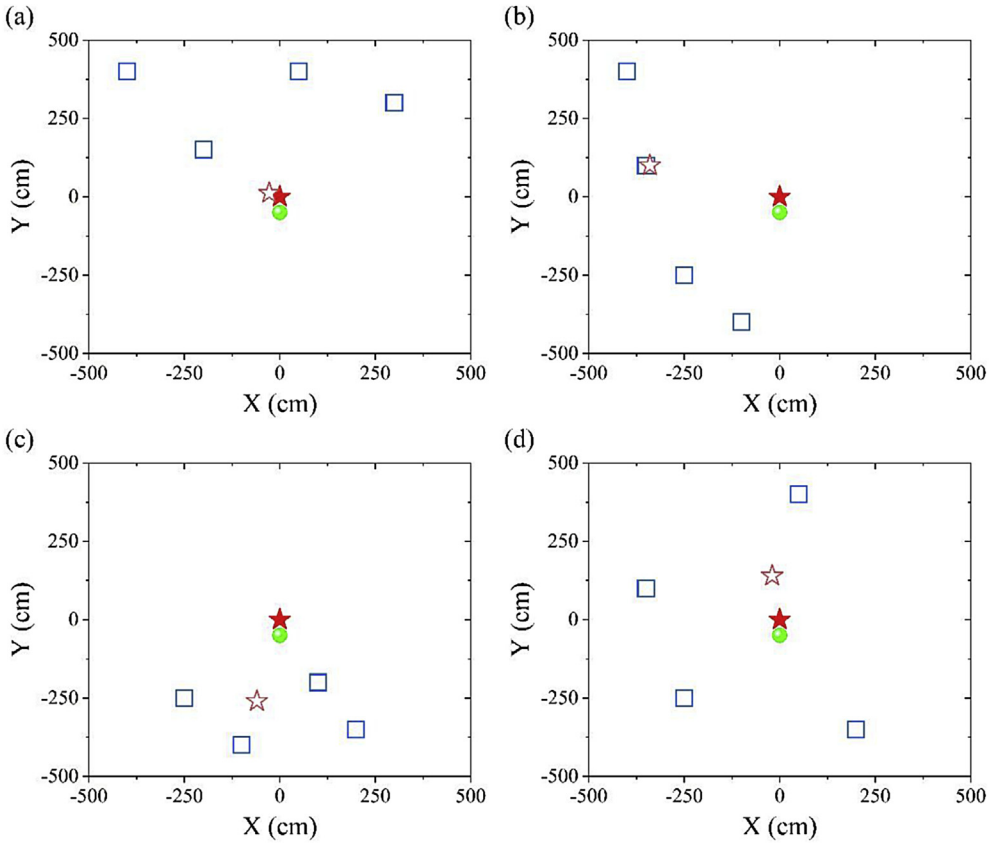

Fig. 22. Calculated source positions with different distributions of the detection positions in Scene B. The detection positions were dispersed (a) on the opposite side of the source from the tree, (b) on one side of the source and the tree, (c) on the same side of the source and the tree, and (d) around the source and the tree. The XY projections of the detection positions are indicated by the blue squares. The actual source position is indicated by the solid red star, and the calculated source position is indicated by the hollow red star. The green ball shows the position of the tree. (For interpretation of the references to color in this figure legend, the reader is referred to the Web version of this article.)

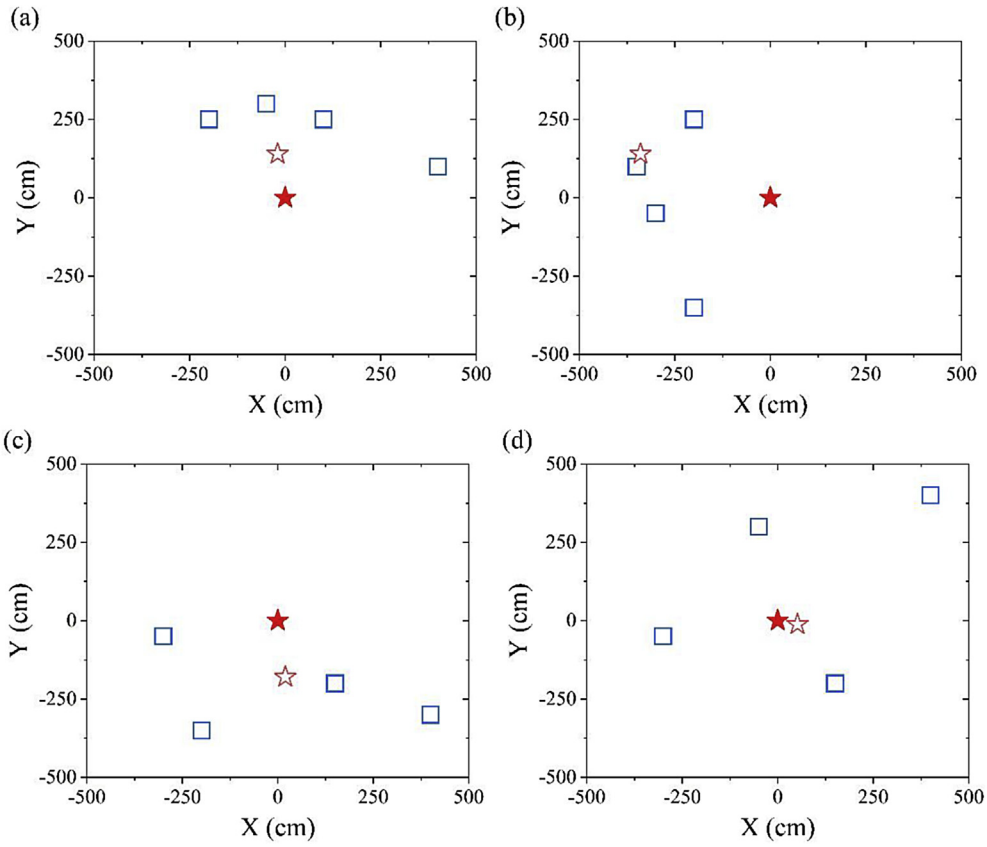

Fig. 23. Calculated source positions with different distributions of the detection positions in Scene C. The detection positions were (a–c) focused on one side of the X axis or the Y axis and (d) dispersed around the source. The XY projections of the detection positions are indicated by the blue squares. The actual source position is indicated by the solid red star, and the calculated source position is indicated by the hollow red star. (For interpretation of the references to color in this figure legend, the reader is referred to the Web version of this article.)

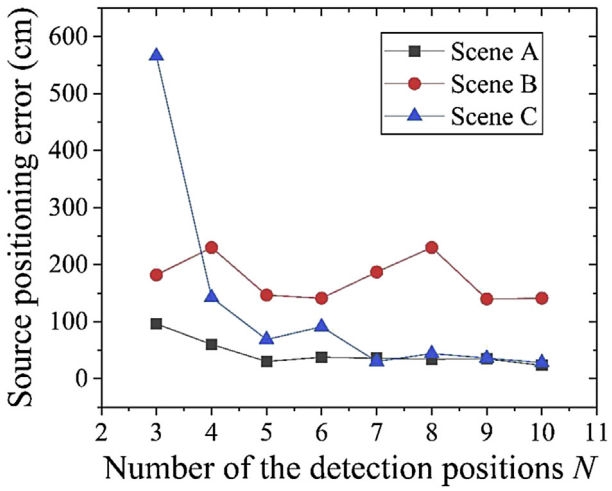

Fig. 24. Source positioning errors in distance with different numbers of detection positions.

of the detection positions, more detection positions should be applied to cover the calculated position and increase the positioning accuracy.

Fig. 20 shows the results of the source positioning errors with different coverage ranges of the detection positions in simulation research Case 5. The source positioning errors increased rapidly with the extension of the coverage range of the detection positions for all kinds of sources. The errors of the 1.33-MeV gamma ray were relatively smaller than those of the others because 1.33-MeV gamma ray has relatively smaller attenuation efficiencies. A $40 \times 40\ m^2$ coverage range of the detection positions with 30 cm of source positioning error is recommended under similar detection conditions as in Case 5.

3.2. Experimental results

First, different distributions of the detection positions in three experimental scenes were studied. Fig. 21 shows the results of the calculated source positions with different distributions of the detection positions in Scene A (^{131}I placed on the grass). Fig. 21(d) in which the detection positions were dispersed around the source shows a higher localization accuracy (distance error of 51 cm) than the other three distributions. These results are consistent with the results in simulation research Case 4.

Fig. 22 shows the results of the calculated source positions with different distributions of the detection positions in Scene B (^{131}I placed next to a tree). Fig. 22(d) in which the detection positions were dispersed around the source does not show the best localization accuracy. The highest localization accuracy (distance error of 30 cm) is shown in Fig. 22(a) in which all the detection positions were dispersed above the X axis. This is because the γ rays emitted from the source were partly shielded by the nearby tree, and the distribution, as shown in Fig. 22(a), that was on the opposite side of the source from the tree was less affected than the other three situations. When trees, buildings, or some big obstacles are present in the suspicious region, arranging the detection positions on one side of the obstacles will improve the localization accuracy.

Fig. 23 shows the results of the calculated source positions with different distributions of the detection positions in Scene C (^{131}I placed in a puddle). Fig. 23(d) in which the detection positions were dispersed around the source shows the highest localization accuracy (distance error of 53 cm) among all distributions. These results are consistent with the simulation results in Case 4 and the experimental results in Scene A.

Then, different numbers of the detection positions were studied for each of the three experimental scenes, and the results are shown in Fig. 24. The positioning errors in Scene C decreased rapidly from 566 cm to 69 cm as the number of detection positions *N* increased from

3 to 5 and then decreased to 28 cm when N increased to 10. The positioning errors in Scene A decreased slowly from 96 cm to 30 cm when N increased to 5 and then decreased slowly to 24 cm when the N increased to 10. At least five detection positions are supposed to be scheduled to minimize the positioning error in real situations, and more detection positions will promote the accuracy to some extent; this is consistent with the simulation results. However, in Scene B the positioning errors were at a relatively high level (141–230 cm), and no obvious trend appeared as the N increased because of the shielding effects from the tree aside the source.

4. Conclusions

The simulation and experimental results indicate that the algorithm developed in this work for locating a lost radioactive source using a UAV radiation monitoring system is feasible. In the experimental scenes, a best localization distance error of 30 cm was retained by this algorithm using our UAV radiation monitoring system, for a 3.7×10^7-Bq ^{131}I source when applied to a suspicious region of 10×10 (m^2). The calculation time is within 0.1 s after a survey flight of 5 min. An obstacle like a tree influenced the positioning accuracy a lot. Arranging the detection positions at one side of the obstacle will considerably improve the positioning accuracy. Future works will be conducted to improve the localization accuracy, including topographic count correction and multiple source localization by employing detectors with higher energy resolution such as $LaBr_3$ or CZT detector.

Acknowledgments

This work was supported by the National Natural Science Foundation of China (Grant No. 11675078), the Primary Research and Development Plan of Jiangsu Province (Grant No. BE2017729), the Fundamental Research Funds for the Central Universities (Grant No. NJ20160034), the Funding of Jiangsu Innovation Program for Graduate Education (Grant No. KYLX16_0353) and the Fundamental Research Funds for the Central Universities.

References

Brewer, E., 2009. Autonomous Localization of 1/R^2 Sources Using an Aerial Platform. MA Thesis, Mechanical Engineerin, Virginia Tech, Blacksburg, VA, USA.
Brown, F.B., 2003. MCNP–A General Monte Carlo N-Particle Transport Code. Los Alamos National Laboratory, Oak Ridge, TN Version 5.
Casanovas, R., Morant, J.J., Salvadó, M., 2014. Development and calibration of a real-time airborne radioactivity monitor using direct gamma-ray spectrometry with two scintillation detectors. Appl. Radiat. Isot. 89, 102–108.
Connor, D., Martin, P.G., Scott, T.B., 2016. Airborne radiation mapping: overview and application of current and future aerial systems. Int. J. Remote Sens. 37 (24), 5953–5987.
Falciglia, P.P., Biondi, L., Catalano, R., Immè, G., Romano, S., Vagliasindi, F.G., 2017. Preliminary investigation for quali-quantitative characterization of soils contaminated with 241Am and 152Eu by low-altitude unmanned aerial vehicles (UAVs) equipped with small size γ-ray spectrometer: detection efficiency and minimum detectable activity (MDA) concentration assessment. J. Soils Sediments 1–11.
Gong, C.H., Zeng, G.Q., Ge, L.Q., Tang, X.B., Tan, C.J., 2014. Minimum detectable activity for NaI (Tl) airborne γ-ray spectrometry based on Monte Carlo simulation. Sci. China Technol. Sci. 57 (9), 1840–1845.
Gunatilaka, A., Ristic, B., Gailis, R., 2007. On localisation of a radiological point source. In: 2007 Information, Decision and Control. IEEE, pp. 236–241.
Han, J., Chen, Y., 2014. Multiple UAV formations for cooperative source seeking and contour mapping of a radiative signal field. J. Intell. Robot. Syst. 74 (1–2), 323–332.
Hanna, D., Sagnières, L., Boyle, P.J., MacLeod, A.M.L., 2015. A directional gamma-ray detector based on scintillator plates. Nucl. Instrum. Methods Phys. Res., Sect. A 797, 13–18.
Howse, J.W., Ticknor, L.O., Muske, K.R., 2001. Least squares estimation techniques for position tracking of radioactive sources. Automatica 37 (11), 1727–1737.
Huang, X., Meng, J., Wang, P., Cao, Y., Tang, X.B., Weng, L.S., Chen, D., 2016. Efficiency calibration and minimum detectable activity concentration of a real-time UAV airborne sensor system with two gamma spectrometers. Appl. Radiat. Isot. 110, 100–108.
Jerry, T., Bryan, K., Kevin, K., 2012. Radiation mapping in post-disaster environments using an autonomous helicopter. Rem. Sens. 4 (12), 1995–2015.
Knoll, G.F., 2010. Radiation Detection and Measurement, fourth ed. Wiley, New York.
Kurvinen, K., Smolander, P., Pöllänen, R., Kuukankorpi, S., Kettunen, M., Lyytinen, J., 2005. Design of a radiation surveillance unit for an unmanned aerial vehicle. J. Environ. Radioact. 81 (1), 1–10.
Luke, P.N., Amman, M., Lee, J.S., Ludewigt, B.A., Yaver, H., 2001. A CdZnTe coplanar-grid detector array for environmental remediation. Nucl. Instrum. Methods Phys. Res., Sect. A 458 (1–2), 319–324.
MacFarlane, J.W., Payton, O.D., Keatley, A.C., Scott, G.P.T., Pullin, H., Crane, R.A., Smilion, M., Popescu, I., Curlea, V., Scott, T.B., 2014. Lightweight aerial vehicles for monitoring, assessment and mapping of radiation anomalies. J. Environ. Radioact. 136, 127–130.
Martin, P.G., Payton, O.D., Fardoulis, J.S., Richards, D.A., Scott, T.B., 2015. The use of unmanned aerial systems for the mapping of legacy uranium mines. J. Environ. Radioact. 143, 135–140.
Martin, P.G., Payton, O.D., Fardoulis, J.S., Richards, D.A., Yamashiki, Y., Scott, T.B., 2016. Low altitude unmanned aerial vehicle for characterising remediation effectiveness following the FDNPP accident. J. Environ. Radioact. 151, 58–63.
Morelande, M., Ristic, B., Gunatilaka, A., 2007. Detection and parameter estimation of multiple radioactive sources. In: 2007 10th International Conference on Information Fusion. vols. 1–7 IEEE.
Pöllänen, R., Toivonen, H., Peräjärvi, K., Karhunen, T., Ilander, T., Lehtinen, J., Rintala, K., Katajainen, T., Niemelä, J., Juusela, M., 2009. Radiation surveillance using an unmanned aerial vehicle. Appl. Radiat. Isot. 67 (2), 340–344.
Rao, N.S.V., Sen, S., Prins, N.J., Prins, N.J., Cooper, D.A., Ledoux, R.J., Costales, J.B., Kamieniecki, K., Korbly, S.E., Thompson, J.K., Batcheler, J., Brooks, R.R., Wu, C.Q., 2015. Network algorithms for detection of radiation sources. Nucl. Instrum. Methods Phys. Res., Sect. A 784, 326–331.
Šálek, O., Matolín, M., Gryc, L., 2018. Mapping of radiation anomalies using UAV mini-airborne gamma-ray spectrometry. J. Environ. Radioact. 182, 101–107.
Sanada, Y., Torii, T., 2015. Aerial radiation monitoring around the Fukushima Dai-ichi nuclear power plant using an unmanned helicopter. J. Environ. Radioact. 139, 294–299.
Sharma, M.K., Alajo, A.B., Lee, H.K., 2016. Three-dimensional localization of low activity gamma-ray sources in real-time scenarios. Nucl. Instrum. Methods Phys. Res., Sect. A 813, 132–138.
Towler, J., Krawiec, B., Kochersberger, K., 2012. Radiation mapping in post-disaster environments using an autonomous helicopter. Rem. Sens. 4 (7), 1995–2015.
Willis, M.J., Skutnik, S.E., Hall, H.L., 2014. Detection and positioning of radioactive sources using a four-detector response algorithm. Nucl. Instrum. Methods Phys. Res., Sect. A 767, 445–452.
Xu, X.C., Rao, N.S.V., Sahni, S., 2010. A computational geometry method for localization using differences of distances. ACM Trans. Sens. Netw. 6 (2), 10.